Compressive sensing-based correlation plenoptic imaging

Isabella Petrelli[1†], Francesca Santoro[1†], Gianlorenzo Massaro[2,3]*, Francesco Scattarella[2,3], Francesco V. Pepe[2,3], Francesca Mazzia[4], Maria Ieronymaki[5], George Filios[5], Dimitris Mylonas[5], Nikos Pappas[5], Cristoforo Abbattista[1‡] and Milena D'Angelo[2,3‡]

[1]Planetek Italia s.r.l. (Italy), Bari, Italy, [2]Dipartimento Interuniversitario di Fisica, Università degli Studi di Bari, Bari, Italy, [3]Istituto Nazionale di Fisica Nucleare, Bari, Italy, [4]Dipartimento di Informatica, Università degli studi di Bari, Bari, Italy, [5]Planetek Hellas E.P.E., Marousi, Greece

Correlation Plenoptic Imaging (CPI) is an innovative approach to plenoptic imaging that tackles the inherent trade-off between image resolution and depth of field. By exploiting the intensity correlations that characterize specific states of light, it extracts information of the captured light direction, enabling the reconstruction of images with increased depth of field while preserving resolution. We describe a novel reconstruction algorithm, relying on compressive sensing (CS) techniques based on the discrete cosine transform and on gradients, used in order to reconstruct CPI images with a reduced number of frames. We validate the algorithm using simulated data and demonstrate that CS-based reconstruction techniques can achieve high-quality images with smaller acquisition times, thus facilitating the practical application of CPI.

KEYWORDS

light-field imaging, Plenoptic Imaging, 3D imaging, correlation imaging, compressive sensing

1 Introduction

Correlation Plenoptic Imaging (CPI) [1–9], is a recently developed approach to plenoptic imaging (also know as light-field imaging), which aims, by exploiting correlations of light intensity, to overcome the strong tradeoff between image resolution and maximum achievable depth of field that affects conventional techniques, based on direct intensity measurements [10–18]. All plenoptic imaging techniques aim at reconstructing the three-dimensional distribution of light in a scene by simultaneously encoding in optically measurable quantities information on the intensity and the distribution of light in given reference plane in the scene. Detection of the propagation direction of light offers several advantages compared to conventional imaging, since it provides high-depth-of-field images of the sample from different perspectives, thus enabling post-acquisition volumetric refocusing without the need for scanning the scene of interest. While in conventional PI spatial and directional information are encoded, usually by means of a microlens array, in the intensity impinging on a single sensor, in CPI they can be retrieved only by measuring spatio-temporal correlations between intensities registered by pixels on two disjoint sensors. In fact, the initial embodiments of CPI [1] were inspired by a previously established correlation imaging technique, called Ghost Imaging (GI): here, a two-dimensional image is obtained by correlating the total intensity transmitted (or reflected) by an object, as measured through a single-pixel (known as bucket) detector, with the signal acquired by a sensor with high spatial resolution that, conversely, collects light that has not

interacted with the object [19–26]. The main difference between GI and CPI lies in the much larger amount of information collected by measuring light correlations on two space-resolving sensors, compared with the single-pixel measurement performed in GI. In GI, in fact, the object can be successfully reconstructed only when it is at focus, whereas CPI can *refocus* the image over a much larger axial depth.

Despite their promising application potentials, CPI and GI share the main drawback of correlation imaging techniques, namely, the need to accumulate statistics (i.e., independent intensity frames) in order to reconstruct the desired correlation signal. In particular, the signal-to-noise ratio (SNR) of CPI and GI images scales like the square root of the number of acquired frames [27–29], but the acquisition time increases linearly in the latter quantity, leading to a necessary compromise between accurate and fast imaging. In the case of GI, many efforts have been made to reduce the sampling rate and enhance the acquisition speed without sacrificing the image quality. Interesting attempts to model the problem of image reconstruction as an optimization problem, following the principles of compressive sensing (CS), have been successfully applied to increase image quality in case of scarce statistics [30,31]. The basic idea behind CS is to employ only a few samples and exploit the sparsity of the acquired signal in some specific domain to reconstructing a high-SNR image [32–35]. From the theoretical point of view, CS is a convex optimization problem, in which one looks for the sparsest signal that minimizes a given cost function. As detailed in the following sections, the choice of a cost function to optimize depends both on the structure of the problem to be faced, and on specific requirements in the reconstructed image (e.g., weighing data-fidelity or sparsity terms, or considering additional noise-related effects).

In this paper, we investigate the feasibility of applying CS inspired techniques to CPI, building on the promising results achieved in compressive GI. We propose a CS-based algorithm that incorporates a regularization term which exploits the sparseness of image gradients as an alternative approach with respect to the conventional correlation-based one. The algorithm, specifically designed for Correlation Plenoptic Imaging, aims at 1) reducing the number of frames necessary to achieve a target image quality, 2) replacing the CPI cross-correlation computation with an optimization process. The paper is organized as follows: in Section 2.1, we recall the basic concepts of Correlation Plenoptic Imaging; in Section 2.2, we introduce a formal description of the proposed CS-based algorithm for CPI reconstruction; in Section 3, the proposed method is investigated numerically; we summarize the results and provide final remarks in Section 4.

2 Materials and methods

2.1 Fundamentals of correlation plenoptic imaging

The CPI technique extends the potentials of GI by enabling one to retrieve combined spatial and directional information without scanning the scene. CPI substantially differs from GI in the fact that both the detectors that register the intensities to be correlated are characterized by spatial resolution. Such a feature has a relevant

implication in the evaluation of correlations, as we are going to explain in the following. Though the results obtained in this work can be generalized to any CPI setup, we refer for the sake of definiteness to the setup that bears the closest analogy to GI, namely, the first one to be proposed [1] and experimentally realized [3], schematically depicted in Figure 1.

We consider a source emitting quasi-monochromatic light with chaotic (pseudothermal) statistics, characterized by negligible spatial coherence on its emission surface; the source is divided in two paths by a beam splitter. One of the beams (the reflected one, in the case depicted in Figure 1) follows path a and directly reaches the detector D_a, which is located at an optical distance z_a from the source, without interacting with the object. The other beam (the transmitted one in Figure 1) follows path b, where it first interacts with a sample, placed at a distance z_b from the source, and considered for simplicity as a planar transmissive object; then, it passes through a lens L of focal length f, placed at a distance z_b' from the sample, which focuses on sensor D_b, at a distance z_b'' from L, an image *of the source*. Three of the distances mentioned in the above description are related by the thin lens equation $1/(z_b + z_b') + 1/z_b'' = 1/f$. For simplicity, we assume henceforth that the two sensors are square, with N_a and N_b pixels per side, respectively. The described CPI setup generalized lensless GI [24] by replacing the "bucket" detector, that collects all the light transmitted by the object in the latter case, with 1) a detector D_b endowed with spatial resolution, 2) a lens that sharply focuses the source on D_b. From the point of view of image formation, each pixel of D_b can be considered as a separate bucket detector: due to the strong defocusing of the object with respect to D_b, light from the whole object contributes to the light intensity measured by each angular pixel. Hence, the whole object contributes to light fluctuations measured by a single pixel on D_b, as would be the case with a bucket detector in GI. In fact, unlike in conventional imaging systems, where the sample is the effective source of chaotic light, in our case the source is the optical element that is optically conjugated (through the lens L) to D_B. Because of this, the correspondence between pixels and object points typical of imaging is replaced, in the CPI scheme in Figure 1, by a correspondence between pixels and source points, where the object acts as a "disturbance" on the optical path. Hence, each *sub-ghost image* of the object, as obtained by correlating a pixel on D_b with the whole D_a, recovers a sub-image formed only by the light emitted by the specific area of the source that is optically conjugated to that pixel.

The correlation of the intensity fluctuations measured by the two detectors can be expressed by the following formula:

$$\Gamma(\boldsymbol{\rho}_a, \boldsymbol{\rho}_b) = \langle \Delta I_a(\boldsymbol{\rho}_a) \Delta I_b(\boldsymbol{\rho}_b) \rangle \tag{1}$$

where $\boldsymbol{\rho}_a$ and $\boldsymbol{\rho}_b$ are the planar coordinates of pixels on detector D_a and D_b, respectively, while ΔI_a and ΔI_b are the temporal intensity fluctuations recorded on the pixels specified in their arguments. The statistical average $\langle \dots \rangle$ can be reconstructed by collecting M frames, in which the object is illuminated by independent chaotic (speckle) patterns. Eq. 1 shows the main difference between GI and CPI: in fact, whereas ghost imaging retrieves the image of the object by measuring correlations between D_a and a bucket detector, CPI makes use of the additional information originating from the spatial resolution of D_b to refocus. In other terms, CPI would reduce to GI if D_b
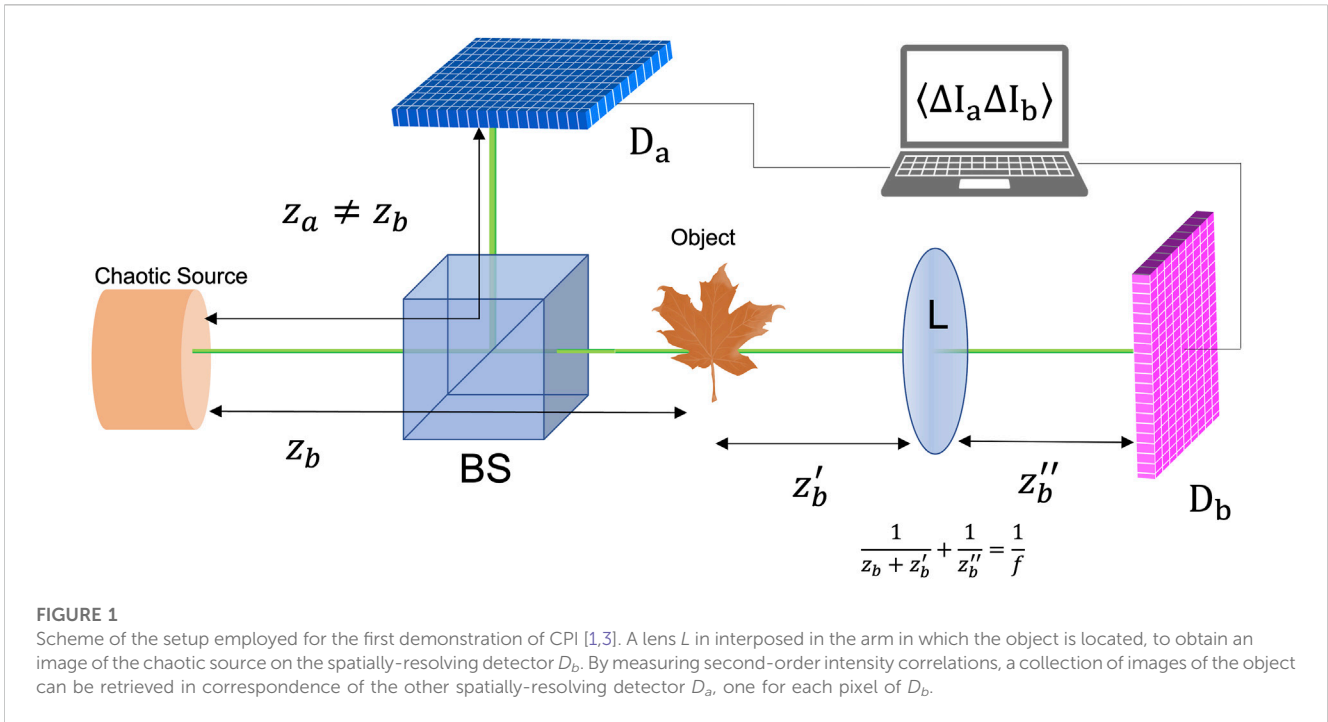
FIGURE 1
Scheme of the setup employed for the first demonstration of CPI [1,3]. A lens *L* in interposed in the arm in which the object is located, to obtain an image of the chaotic source on the spatially-resolving detector D_b. By measuring second-order intensity correlations, a collection of images of the object can be retrieved in correspondence of the other spatially-resolving detector D_a, one for each pixel of D_b.

were composed by a single-pixel detector. Applying the geometrical optics approximation, the correlation function can be expressed in terms of the intensity profile of the chaotic source $\mathcal{F}$ and amplitude transmission function A of the object [1]:

$$\Gamma(\boldsymbol{\rho}_a, \boldsymbol{\rho}_b) \sim \mathcal{F}\left(-\frac{\boldsymbol{\rho}_b}{M}\right)^2 \left| A\left[\frac{z_b}{z_a}\boldsymbol{\rho}_a - \frac{\boldsymbol{\rho}_b}{M}\left(1 - \frac{z_b}{z_a}\right)\right] \right|^2. \quad (2)$$

Therefore, in the geometrical approximation, the correlation function, which is defined in the 4D space of the detector coordinates, reduces to the product of the image of the source, as retrieved by D_b, with images of the object calculated as a function of a linear combination of the coordinates on both detectors. As anticipated, in fact, each image obtained by fixing a value for $\boldsymbol{\rho}_b$ corresponds to an image of the object, scaled and shifted according to the chosen value of $\boldsymbol{\rho}_b$ and the coefficients of the linear combination. When the object is placed in $z_b = z_a$, as is the case in conventional GI, the sub-images are neither shifted nor rescaled from one another, and integration over $\boldsymbol{\rho}_b$ (*i.e.*, sum of all sub-images) gives the standard ghost image. However, this operation provides a *focused* image only when $z_a = z_b$ (more precisely, when the difference of the two distances is smaller than the depth of field defined by the light wavelength and the source numerical aperture, as seen from the object plane [1,3]). The situation changes if the object is displaced of an arbitrary quantity from the focused plane. In this case, the operation of integrating the Γ function over $\boldsymbol{\rho}_b$ to obtain a ghost image as in the previous case is detrimental. This because being $\Gamma_{\boldsymbol{\rho}_b}(\boldsymbol{\rho}_a)$ (at fixed $\boldsymbol{\rho}_b$) a different perspective of the object, the out of focus condition misaligns each of them and the integration gives a blurred image. However, Eq. 2 provides a way to reconstruct (*refocus*) [36] the object by exploiting spatial resolution on D_b, which entails knowledge of the source point $-\boldsymbol{\rho}_b/M$ from which the scene is

illuminated. Intuitively, refocusing is based on the geometrical correspondence between points on the object plane and detection coordinates $\boldsymbol{\rho}_a$ and $\boldsymbol{\rho}_b$, as established by Eq. 2; such correspondence can be inverted to apply a coordinate transformation on Γ so that, in the transformed coordinate system, all sub-images are properly aligned to avoid blurring when they are summed together. Thus, the function

$$\Sigma_{\text{ref}}(\boldsymbol{\rho}_a) = \int \text{d}^2\boldsymbol{\rho}_b \Gamma\left[\frac{z_a}{z_b}\boldsymbol{\rho}_a - \frac{\boldsymbol{\rho}_b}{M}\left(1 - \frac{z_a}{z_b}\right), \boldsymbol{\rho}_b\right] \sim |A(\boldsymbol{\rho}_a)|^2. \quad (3)$$

provides, in the geometrical optics limit, a faithful image of the object, regardless of its position. In fact, as one can easily check, if the coordinate transformation on the first argument of Γ is applied on Eq. 2, the $\boldsymbol{\rho}_b$-dependence is conveniently lost. Finite wavelenghts, instead, set limits related to wave optics [3]. It is worth noticing that, in order to get a properly refocused image, one should know with sufficient precision both the source-to-D_a distance z_a and the source-to-object distance z_b. However, a likely situation is the one in which z_a is precisely determined by the choice of the experimental setup, while the value of z_b is unknown: in this case, the parameter z_b in Eq. 3 can be adjusted in order to maximize sharpness of the refocused image, thus also providing a way to estimate of the object distance.

The extension to CPI of the CS-based reconstruction algorithms designed for chaotic GI [30,31] is not trivial. The main difference lies precisely in the presence of the linear transformation 3) to be applied to the correlation function, and the subsequent integration over the "directional" detector D_b. These algorithms rely on the minimization of an objective function, whose formulation must incorporate in a proper way the linear transformation of the Γ function in the aforementioned equation.

2.2 Compressive correlation plenoptic imaging

Since the application of CS to CPI can be considered as a generalization of its application to GI, we employ a notation that makes the parallelism between the two imaging techniques more evident. After defining as $I_j^{(m)}(x_j, y_j)$ the intensity registered in the mth frame, with $m \in [1, \ldots, M]$, by the pixel in position $\boldsymbol{\rho}_j = (x_j, y_j)$ on the detector D_j (with $j = a, b$), we call

$$\Delta I_j^{(m)}(x_j, y_j) = I_j^{(m)}(x_j, y_j) - \frac{1}{M} \sum_{k=1}^M I_j^{(k)}(x_j, y_j) \quad \text{with } j = a, b,$$
(4)

the corresponding intensity fluctuation, where the second term is an estimate of the mean intensity. The correlation function Γ, estimated after collecting m frames, thus reads

$$\Gamma_{(x_b, y_b)}(x, y) = \frac{1}{M} \sum_{m=1}^M \Delta I_a^{(m)}(x, y) \Delta I_b^{(m)}(x_b, y_b).$$
(5)

As already mentioned, the term $\Delta I_b^{(m)}(x_b, y_b)$ plays the role of the signal collected by a bucket detector: depending on the specific pixel (x_b, y_b), different sub-images Γ_{x_b, y_b} are indeed obtained by cross-correlating the same sensing matrix (as obtained by stacking $\Delta I_a^{(m)}(x, y)$, as better detailed in the following) with different arrays of bucket signals. Based on the similarity with GI, we employ the approach of *differential* GI [37], as already followed in Ref. [7] in a slightly different CPI context, and perform the replacement

$$\Delta I_b^{(m)}(x_b, y_b) \rightarrow \tilde{\Delta} I_b^{(m)}(x_b, y_b) = \Delta I_b^{(m)}(x_b, y_b) \\ - \frac{\sum_{k=0}^M \Delta I_b^{(m)}(x_b, y_b) \Delta I_{a,TOT}^{(k)}}{\sum_{k=0}^M \left(\Delta I_{a,TOT}^{(k)}\right)^2} \Delta I_{a,TOT}^{(m)},$$
(6)

with $\Delta I_{a,TOT}^{(m)} = \sum_{(x_a, y_a)} \Delta I_a^{(m)}(x_a, y_a)$. Differential GI, in fact, has the well-known property of improving the signal-to-noise ratio of the reconstructed image by employing a data-processing approach that simply replaces the conventional bucket signal with an optimized signal. The refocusing algorithm eventually realigns all images, which contribute to the overall one in Eq. 3. The previous considerations are at the basis of the CS generalization to CPI. Let us consider a fixed pixel (x_b, y_b), which can also be conveniently labelled with $i \in \{1, \ldots, N_b^2\}$, of the detector D_b: the corresponding image, consists in a linear superposition of fluctuation patterns $\Delta I_a^{(m)}(x, y)$, weighted by $\tilde{\Delta} I_b^{(m)}(x_b, y_b)$. Following the CS scheme, each of the M patterns $\Delta I_a^{(m)}(x, y)$, consisting in $N_a \times N_a$ matrices, is reshaped into a vector with components $\mathcal{I}_a^{(m)}[j]$, with $j \in \{1, \ldots, N_a^2\}$ labelling the pixel. The $M \times N_a^2$ *measurement matrix* is constructed by stacking all the vectorized light patterns:

$$\mathcal{A} = \begin{bmatrix} \mathcal{I}_a^{(1)}[1] & \cdots & \mathcal{I}_a^{(1)}[N_a^2] \\ \vdots & \ddots & \vdots \\ \mathcal{I}_a^{(M)}[1] & \cdots & \mathcal{I}_a^{(M)}[N_a^2] \end{bmatrix}.$$
(7)

Similarly, the $M \times 1$ *measurement vector* corresponding to the ith pixel in position (x_b, y_b) is obtained by stacking all the bucket signals

$$\mathcal{B}_i = \left(\tilde{\Delta} I_b^{(1)}(x_b, y_b), \ldots \tilde{\Delta} I_b^{(M)}(x_b, y_b) \right)^T$$
(8)

Notice that while the measurement vectors depend on the particular pixel of D_b under analysis, the measurement matrix is independent of such pixels. Therefore, the measurement process imposes a generally different matrix constraint on each out-of-focus image. If we indicate with γ_i the flattened version of $\Gamma_{(x_b, y_b)}$, these constraints read

$$\mathcal{A}\gamma_i = \mathcal{B}_i, \quad \text{for all } i \in \{1, \ldots, N_b^2\}.$$
(9)

In principle, at least $M = N_a^2$ measurements are required to determine the solution of the above equation. In practice, since the intensity patterns are not independent from each other, a number $M \gg N_a^2$ of measurements is needed to obtain a satisfactory outcome. The standard linear reconstruction process makes no assumptions on the target object, while any prior information on its structure would significantly reduce the number of measurements. For most natural images such information exists, since natural images turn out to be *sparse* when represented in specific domains (such as the discrete Fourier transform, the discrete cosine transform, or the gradient domain) [38], in the sense that the number of coefficients by which they are determined is much smaller than the general case.

Before defining the objective function, and therefore the complete minimization problem to be tackled, it is worth noticing that the latter must keep track of the refocusing process 3), leading to the target image on which prior knowledge exists. On the other hand, constraints are formulated in terms of the out-of-focus images. Refocusing cannot be reduced to a matrix multiplication, and depends on the coordinate of pixels on the detector D_b. To solve this issue and recast the problem into a more tractable one, we reverse the standard workflow. Since refocusing amounts to a reassigning the coordinates on detector D_a based on the values of (x_b, y_b), we perform such a remapping on top of the cross-correlation step that we aim to replace. We start by defining the "refocused Γ" as

$$\Gamma_R(x, y) = \sum_{(x_b, y_b)} \frac{1}{M} \sum_{m=1}^M R_{(x_b, y_b)}^{(m)}(x, y) \tilde{\Delta} I_b^{(m)}(x_b, y_b),$$
(10)

with

$$R_{(x_b, y_b)}^{(m)}(x, y) = \Delta I_a^{(m)}\left(\frac{z_a}{z_b} x_a - \frac{x_b}{M}\left(1 - \frac{z_a}{z_b}\right), \frac{z_a}{z_b} y_a - \frac{y_b}{M}\left(1 - \frac{z_a}{z_b}\right) \right)$$
(11)

The updated workflow leads to a refactoring of the constraints encoding the measurements. In particular, Eq. 9 is replaced by

$$\mathcal{A}_i^R \gamma_R = \mathcal{B}_i, \quad \text{for all } i \in \{1, \ldots, N_b^2\},$$
(12)

where the $M \times N_a^2$ objects $\mathcal{A}_i^R$ are obtained by stacking the M flattened *refocused* light patterns $R_{(x_b, y_b)}^{(m)}(x, y)$, in the same way as $\mathcal{A}$ is obtained from $\Delta I_a^{(m)}(x, y)$. The possibility of expressing all the constraints in terms of the same target image γ_R is earned at the expense of having different sensing matrices for each pixel on D_b.

The CS formulation in terms of an optimization problem, for which efficient algorithms exist, involves the minimization of an objective function given by the sum of two terms: a data fidelity term,

FIGURE 2
Graphical representation of the CS optimization procedure defined by Eq. 15.
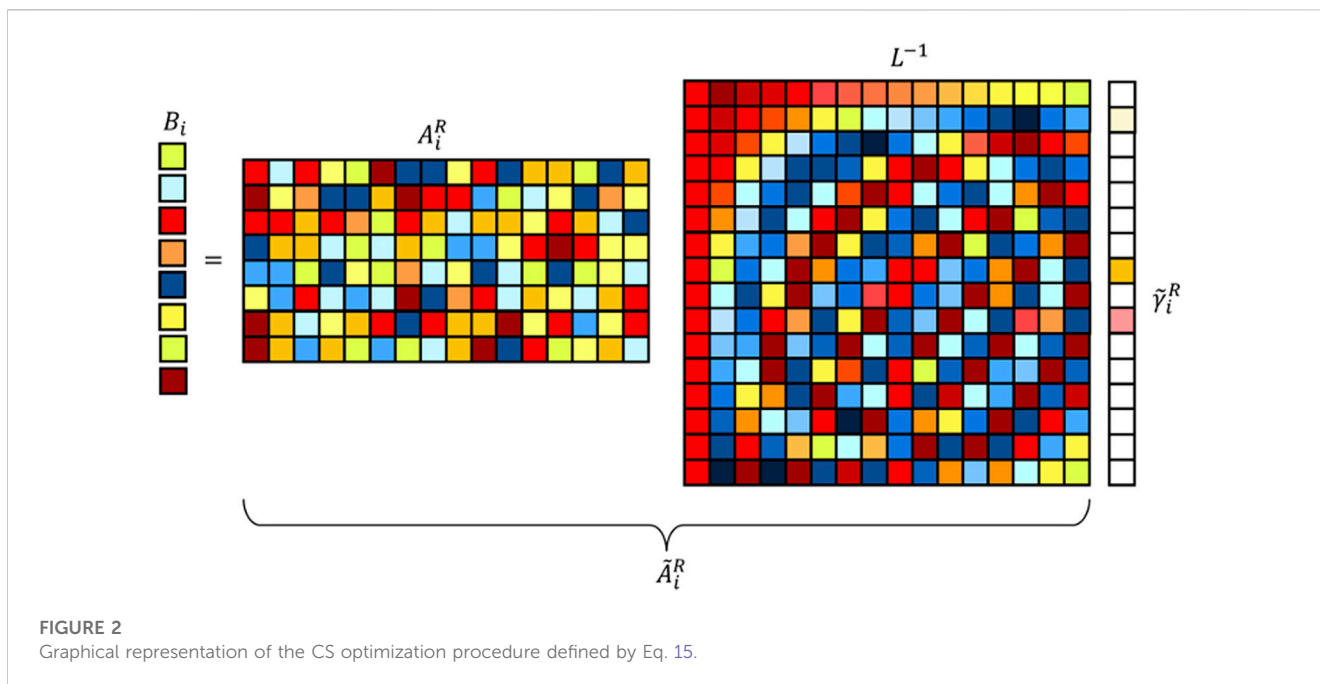
encoding the constraints, and a regularization term, which expresses prior information of the object to be detected. The solution of the problem, representing the optimal reconstructed image, reads

$$\hat{\gamma}_R^i = \arg\min_{\gamma_R} \left\{ \frac{1}{2} \|\mathcal{A}_i^R \gamma_R - \mathcal{B}_i\|_2^2 + \lambda \mathcal{R}(\gamma_R) \right\}, \qquad (13)$$

with $\|v\|_2$ the square-rooted sum of the absolute squared vector components. The parameter λ controls the balance between the constraint and the regularization term $\mathcal{R}(\gamma_R)$. The choice $R(\gamma_R) = \|L\gamma_R\|_0$, with the quasi-norm $\|v\|_0$ counting the number of non-vanishing elements of v, promotes the sparsity of γ_R in a given transform domain L. In the CS framework, under certain conditions (including sparsity of $L\gamma_R$ and incoherence of L and A_i^R), one can replace the $\|v\|_0$ with the its convex envelope $\|v\|_1$, namely, the sum of the absolute elements of v norm, leading to the convex optimization formulation

$$\hat{\gamma}_R^i = \arg\min_{\gamma_R} \left\{ \frac{1}{2} \|\mathcal{A}_i^R \gamma_R - \mathcal{B}_i\|_2^2 + \lambda \|L\gamma_R\|_1 \right\}, \qquad (14)$$

with L operator performing the transform in the domain where the image is supposed to be sparse. The above optimization problem can be recast in terms of the image transform $\tilde{\gamma}_R^i = L\gamma_R^i$ by absorbing the sparsifying matrix L in the sensing matrix, to obtain

$$\hat{\tilde{\gamma}}_R^i = \arg\min_{\tilde{\gamma}_R} \left\{ \frac{1}{2} \|\tilde{\mathcal{A}}_i^R \tilde{\gamma}_R - \mathcal{B}_i\|_2^2 + \lambda \|\tilde{\gamma}_R\|_1 \right\}, \qquad (15)$$

with $\tilde{\mathcal{A}}_i^R = \mathcal{A}_i^R L^{-1}$. The procedure is schematically illustrated in Figure 2. Once the minimization problem is solved, the image in the spatial domain is obtained as $\hat{\gamma}_R^i = L^{-1}\hat{\tilde{\gamma}}_R^i$.

Many established CS reconstruction algorithms exploit the prior knowledge that natural images are sparse in a given domain, such as discrete cosine transform (DCT) (see Ref. [30] for an application to GI). However, image signals are usually reshaped into one-dimensional signals, thus hiding part of the structure

information. In this context, we explore a regularization term related to the total variation (TV) of the image, namely, the norm of the image gradient. CS-based TV regularization methods exploit the sparseness of the image gradients in the *spatial* domain. More complex solutions include more than one regularization term, promoting both sparsity of DCT or Fourier transform and image gradients. Possible regularization strategies involve the functions outlined below:

- **Case 1**: sparse structure is expected in a transform domain such as the DCT. The inverse transform matrix represents the 2D inverse DCT, applied to the minimization outcome to obtain the reconstructed two-dimensional image
- **Case 2a**: as well-known from previous works [39–41], the discrete gradient of natural images along the horizontal and vertical directions are sparse, therefore TV regularization can be used, as firstly proposed by Rudin-Osher-Fatemi [42]. While the original formulation is referred to as the isotropic total variation, an anisotropic formulation was also addressed in the literature [43],

$$\mathcal{R}_{TV}(\gamma_R) := \|D\gamma_R\|_{2,1} = \left\| \sqrt{|D_x\gamma_R|^2 + |D_y\gamma_R|^2} \right\|_1, \qquad (16)$$

$$\mathcal{R}_{TV,an}(\gamma_R) := \|D\gamma_R\|_1 = \|D_x\gamma_r\|_1 + \|D_y\gamma_r\|_1, \qquad (17)$$

Where D_x and D_y denote the horizontal and vertical discrete partial derivatives, respectively, and $D = (D_x, D_y)$ is the discrete gradient operator. The discrete partial derivatives are approximated by first order forward differences. From the numerical point of view, the exact total variation term can make the problem intractable. However, after some manipulations, it is possible to recast the optimization problem which includes the anisotropic approximation of the TV term to the standard form by means of an extended model, with $\gamma_{ext} = \left[(D_x\gamma_R)^T, (D_y\gamma_R)^T \right]^T$ and sensing matrix $\tilde{\mathcal{A}}_i^{R,ext} = \left[\frac{1}{2}\mathcal{A}_i^R D_x^{-1}, \frac{1}{2}\mathcal{A}_i^R D_y^{-1} \right]$.
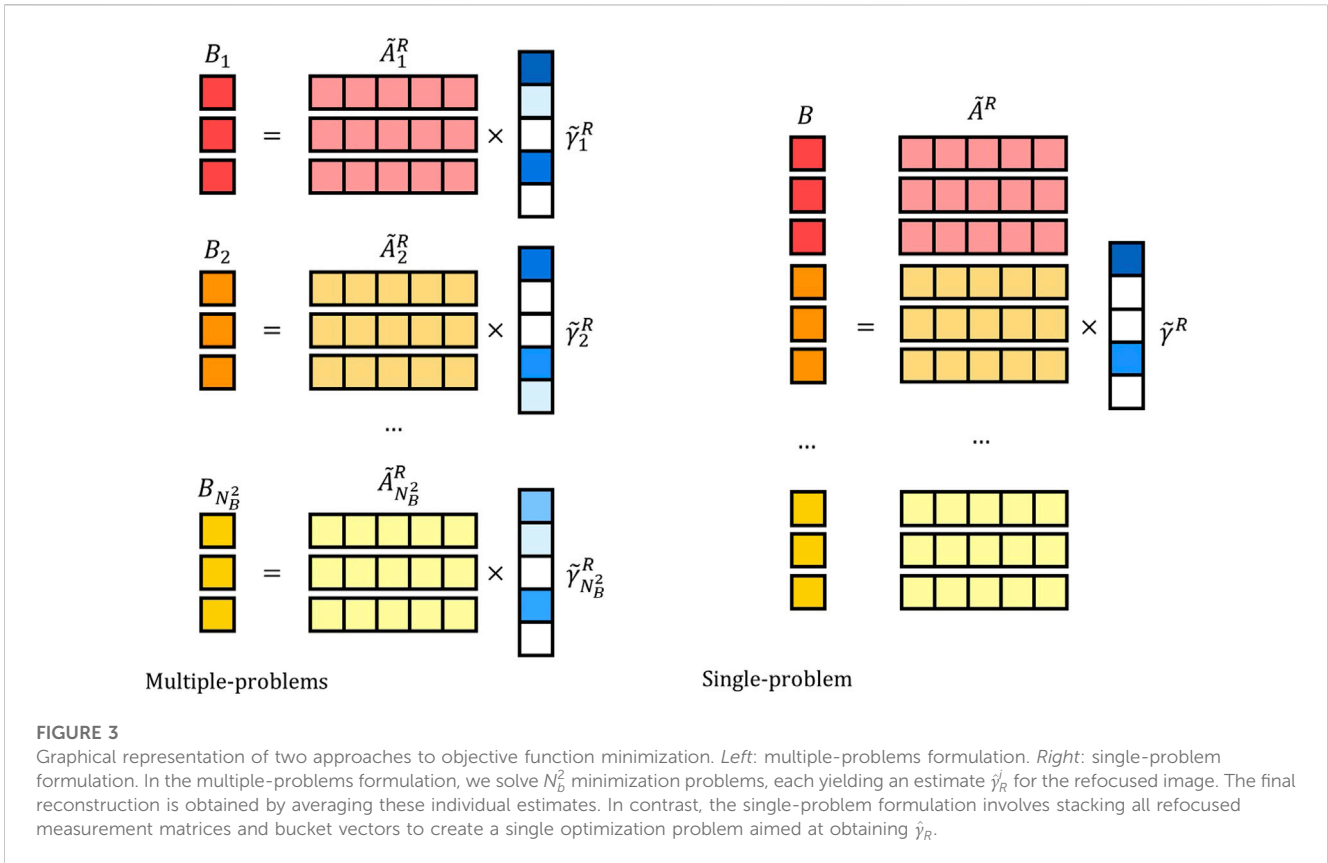
FIGURE 3
Graphical representation of two approaches to objective function minimization. *Left*: multiple-problems formulation. *Right*: single-problem formulation. In the multiple-problems formulation, we solve N_b^2 minimization problems, each yielding an estimate $\hat{y}_R^i$ for the refocused image. The final reconstruction is obtained by averaging these individual estimates. In contrast, the single-problem formulation involves stacking all refocused measurement matrices and bucket vectors to create a single optimization problem aimed at obtaining $\hat{y}_R$.

- **Case 2b**: other edge-detection operators were considered in previous research [44], such as the Laplacian operator

$$\mathcal{R}_{Lapl}(\gamma_R) := \|\mathrm{D}_x^2 \gamma_R + \mathrm{D}_y^2 \gamma_R\|_1. \qquad (18)$$

The reason why we consider a second-order regularization term is due to the fact that the problem can be easily recast to a standard form without extending the model, but just considering the modified sensing matrix $\mathcal{A}_i^{Lapl} = \mathcal{A}_i^R (\mathrm{D}_x^2 + \mathrm{D}_y^2)^{-1}$. We consider the central difference approximation of the second derivatives.

The previously described regularization terms can be combined with each other (here, we limit our analysis to the anisotropic approximation of the TV and to the Laplace operator), at the expense of the computational complexity. The reason is twofold: the optimal choice of the regularization parameters is usually a non-trivial task, and recasting it to the standard form, for which efficient solvers exist, is possible only by extending the model.

There is one final element to consider regarding the shape of the objective function. Thus far, we have formulated N_b^2 independent optimization problems, with each one corresponding to a distinct D_b pixel. However, the image to be reconstructed remains consistent across these manifold problems. This understanding prompts the exploration of two conceivable approaches: the "multiple-problems" approach and the "single-problem" strategy.

The multiple-problems approach adheres more closely to the original workflow, where each distinct perspective or refocused image (corresponding to individual pixels of D_b) is reconstructed independently: through correlation in the original approach, solving a minimization problem in the CS-based one. Subsequently, these

N_b^2 minimization problems yield a set of estimates, denoted as $\hat{y}_R^i$, each targeting the same object of interest. In this paradigm, the final reconstructed image, $\hat{y}_R$, is derived by a straightforward averaging of the outcomes. Notably, this method presents certain merits, as its inherent parallelizability, as well as its manageable computational complexity due to the relatively modest size of each individual optimization problem and the possibility of reconstructing each point of view.

On the other hand, the single-problem formulation exploits the fundamental insight that, once the sensing matrix is refocused *a priori*, we are effectively striving to reconstruct the same object image from multiple viewpoints. This observation enables us to join the various optimization problems by merging the sensing matrices, as well as the corresponding bucket measurements. From an implementation standpoint, this means stacking all the refocused measurement matrices and all the measurement vectors: a graphical explanation is provided in Figure 3. Consequently, the single-problem approach entails solving one optimization problem, with the objective of obtaining the sparsest image, $\hat{y}_R$. In this approach, each sub-image effectively serves as a measurement of the same underlying object. The notable advantage of this strategy lies in its potential to leverage a multitude of measurements to enhance the algorithm convergence, thereby leading to improved reconstruction quality.

However, it is worth recognizing that the single-problem formulation comes with a challenge: The stacking of several sensing matrices and associated measurements vectors leads to the creation of large matrices, which, in turn, increases the computational complexity. Ultimately, the choice between the

multiple-problems and single-problem formulations should be the result of a trade-off between computational complexity and reconstruction quality.

3 Numerical results

The multiple-problems and single-problem strategies are tested on simulated datasets accounting for source statistics and field propagation. The CS-CPI algorithm was implemented in Python. Specifically, we utilized the scikit-learn library, whose modules encompasses a variety of linear models, including Lasso [45]. The standard reconstruction obtained by correlating a large number of frames (N = 15,000) is taken as the ground truth, a random subset of M frames is extracted from the collection to test CS procedures. To quantify the size of the subset, we consider two parameters: the total number of measurements over the total number of "spatial" pixels, $\alpha = M/N_a^2$, and the number of "directional" pixels per side N_b. In the single-problem formulation, N_b plays a specifically important role in the reconstruction process, since the presence of multiple viewpoints increase the size of the sensing matrix.

The chosen quality metric is the Structural SIMilarity (SSIM) index [46]. Consider x and y two non-negative image signals. If x is supposed to be the reference with perfect quality, then the similarity measure is a quantitative measurement of the quality of the second signal. In this context, the SSIM is defined as

$$SSIM(x, y) = [l(x, y)]^\omega \cdot [c(x, y)]^\phi \cdot [s(x, y)]^\psi, \quad (19)$$

where the similarity measurement is split into three comparisons: luminance $l(x, y)$, contrast $c(x, y)$ and structure $s(x, y)$. The three functions are defined as

$$l(x, y) = \frac{2\mu_x\mu_y + C_1}{\mu_x^2 + \mu_y^2 + C_1}, \quad c(x, y) = \frac{2\sigma_x\sigma_y + C_2}{\sigma_x^2 + \sigma_y^2 + C_2},$$
$$s(x, y) = \frac{\sigma_{xy} + C_3}{\sigma_x\sigma_y + C_3}. \quad (20)$$

The constants $C_i = (K_i L)^2$, with $i = 1, 2, 3$, $K_i \ll 1$ and L the dynamic range of the pixel values, are included to avoid instabilities when the denominators are close to zero. Moreover, μ_i (with $i = x, y$) is the mean intensity, σ_i the standard deviation and σ_{xy} the covariance.

The definition above satisfies the following conditions:

- Simmetry: $SSIM(x, y) = SSIM(y, x)$,
- Boundedness: $SSIM(x, y) \leq 1$,
- Unique maximum: $SSIM(x, y) = 1$ if and only if $x = y$.

Finally, the exponents $\omega > 0$, $\phi > 0$ and $\psi > 0$ are parameters used to adjust the relative importance of the three components. In the following, we set $\omega = \phi = \psi = 1$ and $C_3 = C_2/2$, $K_1 = 0.01$ and $K_3 = 0.03$.

3.1 Case 1: Sparsity in the DCT domain

Since natural images tend to be compressible in the DCT domain, we solve the minimization problem encoded in Eq. 15 using standard convex programming algorithms (e.g., the coordinate descent algorithm). Multiple-problems and single-problem strategies have both been tested. A random sample of M = 225 frames, corresponding to α = 0.05, is extracted and used for the reconstruction. Following this approach, the CS-CPI algorithm improves the reconstruction quality, as highlighted by the results reported in Figure 4. The left panel reports the value of the structural similarity index as a function of the regularization parameter in the CS-CPI case, compared with the value of the correlation in the standard case. Panels on the right compares the reconstruction obtained through cross-correlation with the results obtained with the CS-CPI algorithm, for different values of the parameter λ.
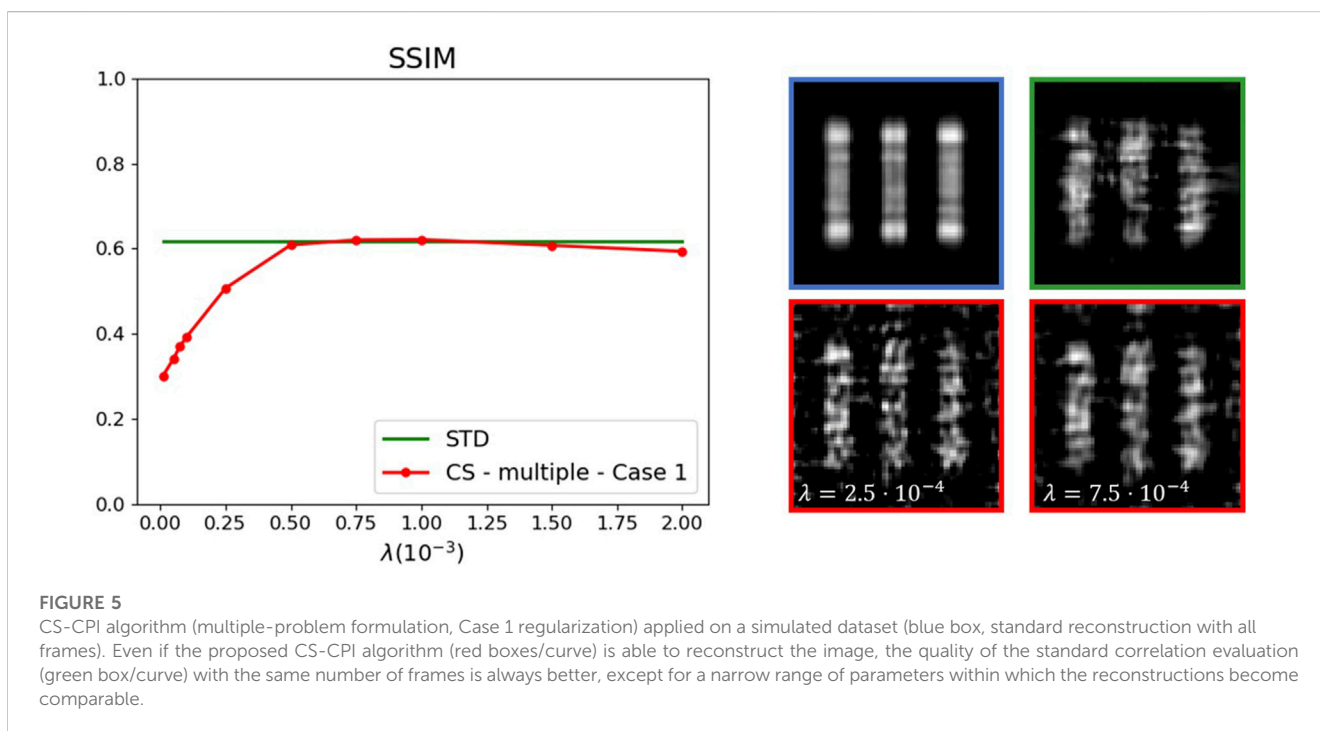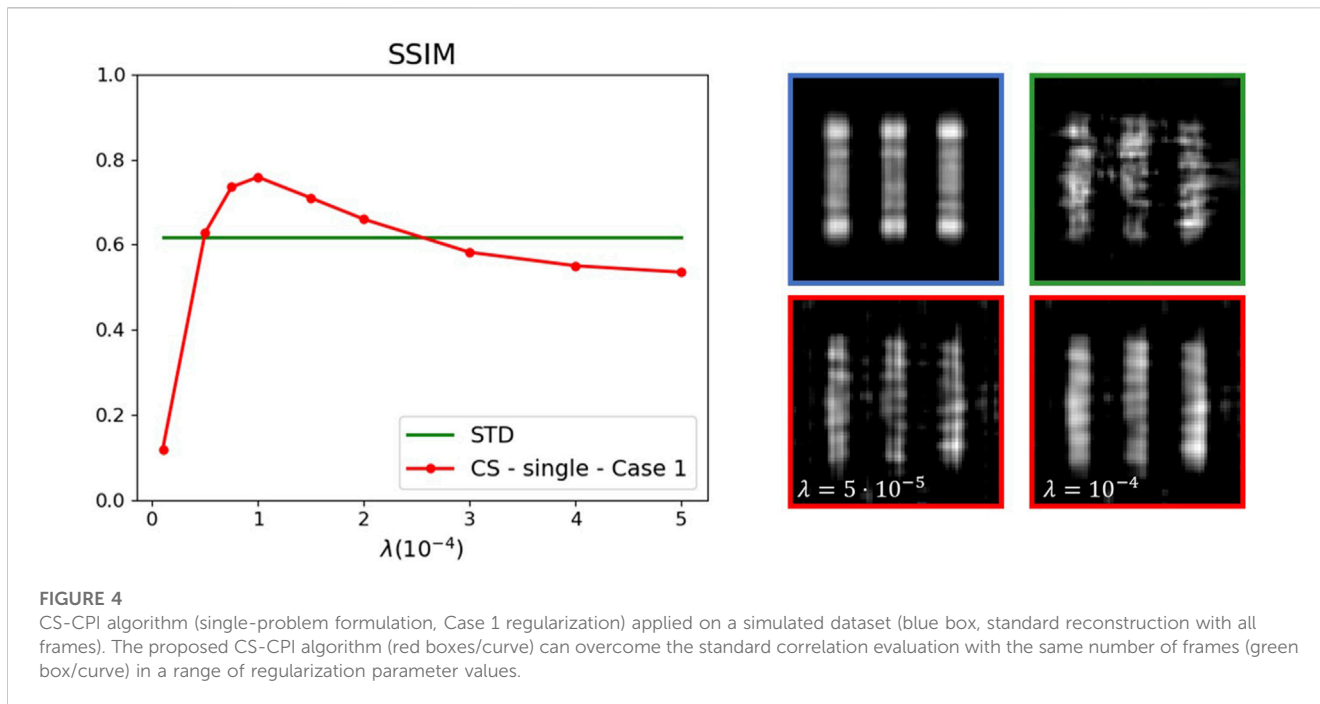
This strategy entails an obvious drawback: huge matrices are involved in the minimization problem, with $\tilde{A}^R$ characterized by MN_n^2 rows and N_n^2 columns. The number of rows becomes easily unmanageable even when a small fraction of the available frames is considered. A possible solution involves parallelization of the algorithm: the rows of $\tilde{A}^R$ are randomly extracted, along with the corresponding ones from $\mathcal{B}$, thus creating separate sub-problems. Each sub-problem can be solved independently from the others, thus leading to different solutions. The process is then complemented by a final average. In any case, the results we obtained demonstrate that a reconstruction strategy based on CS guarantees an improvement in the reconstructed image quality.

The performance of the multiple-problems strategy is not as good as the single-problem one, as expected. The resulting image quality of the two procedures becomes comparable by doubling the frames used for the multiple problems (α = 0.1). As shown in Figure 5, the CS-CPI reconstruction is always poorer than the one obtained through the standard correlation-based evaluation with the same number of frames, except for a narrow range of parameters within which the quality of the two reconstructions become comparable.

In the context of CS, the regularization parameter optimization is a challenging task due to the need for prior knowledge of ideal outcomes. The most suitable parameter is greatly influenced by both the observation model and the specific subject of interest. Consequently, there is no universally applicable method for fine-tuning regularization parameters.

The regularization parameter λ, a trade-off between sparsity and data fidelity, is expected to affect the quality of the image reconstruction Yang et al. [47]. The numerical experiments conducted to assess the sensitivity of λ on the reconstructed image quality (whose results are encoded in Figures 4, 5) show that an optimal λ value exists that yields the best performance in image reconstruction. From Eq. 15, which encapsulates the essential trade-off in CS, the first term primarily serves the purpose of fitting the measured data to reconstruct the image vector, whereas the secon term controls its degree of sparsity. A larger λ places more emphasis on enforcing sparsity within the object, effectively suppressing unsparse image noise. Conversely, a smaller λ has the opposite effect, allowing for the preservation of finer details of the object.

Generally, it is not granted that the CS-based reconstruction outperforms the standard one. The performance of CS algorithms depend on several factors including the properties of the measurement matrix, excessive noise in the measurements, convergence issues in the optimization algorithm or spurious correlations in the measurement matrix.
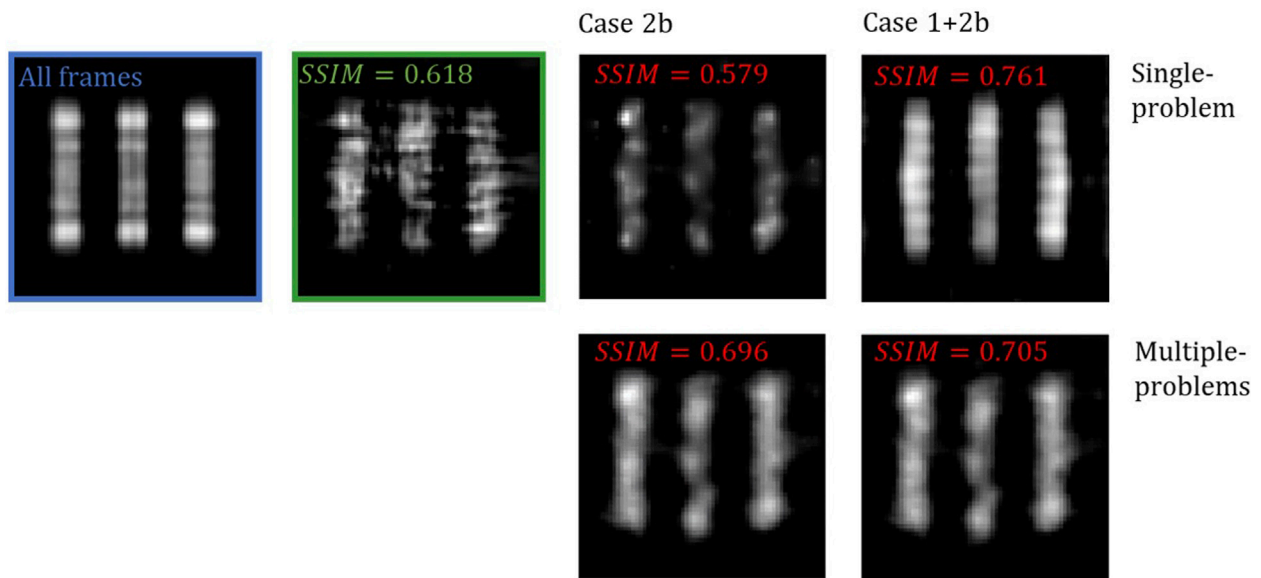
FIGURE 4
CS-CPI algorithm (single-problem formulation, Case 1 regularization) applied on a simulated dataset (blue box, standard reconstruction with all frames). The proposed CS-CPI algorithm (red boxes/curve) can overcome the standard correlation evaluation with the same number of frames (green box/curve) in a range of regularization parameter values.

FIGURE 5
CS-CPI algorithm (multiple-problem formulation, Case 1 regularization) applied on a simulated dataset (blue box, standard reconstruction with all frames). Even if the proposed CS-CPI algorithm (red boxes/curve) is able to reconstruct the image, the quality of the standard correlation evaluation (green box/curve) with the same number of frames is always better, except for a narrow range of parameters within which the reconstructions become comparable.

## 3.2 Case 2: Sparsity in the gradient domain

As discussed in Section 2.2, we tested a version of the CS-based reconstruction algorithm for CPI that incorporates sparsity of image gradients as a regularization term. Specifically, we considered the anisotropic TV approximation (Case 2a) and the Laplacian (Case 2b). Furthermore, we explored the combination of regularization terms, imposing sparsity on both the DCT and the gradients. Also in this context, we tested both the single-problem

and multiple-problems strategies. The same random sample of $M = 225$ frames, corresponding to $\alpha = 0.05$, used in Case 1 was also used in this second case and employed for the reconstruction. However, the performance of the reconstruction algorithm in case 2a (anisotropic approximation of the TV term with and without the DCT term) is not satisfying, hence the results are not shown. In particular, in order to obtain a sufficiently good reconstruction (in any case worse than that obtained by correlations), it is necessary to increase the number of frames

FIGURE 6
CS-CPI algorithm results (first row: single-problem formulation, second row: multiple-problems formulation. Case 2b with and without DCT regularization). The proposed CS-CPI algorithms can overcome the standard correlation evaluation with the same number of frames (green box) in all cases except Case 2b (single-problem formulation), as evident from the structural similarity index reported in the images. The regularization parameters used for the reconstruction are: $\lambda = 2.5 \cdot 10^{-5}$ (single-problem Case 2b), $\lambda = 5 \cdot 10^{-5}$, $\gamma = 2.5 \cdot 10^{-4}$ (single-problem, Case 1+2b), $\lambda = 5 \cdot 10^{-4}$ (multiple-problems, Case 2b), $\lambda = 5 \cdot 10^{-4}$, $\gamma = 2.5 \cdot 10^{-4}$ (multiple-problems, Case 1+2b). (SSIM values in figure updated).
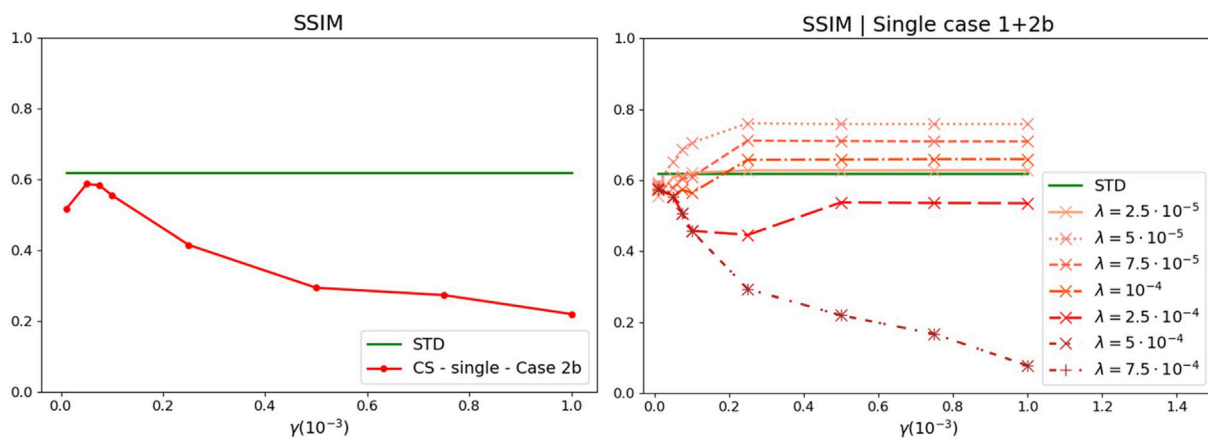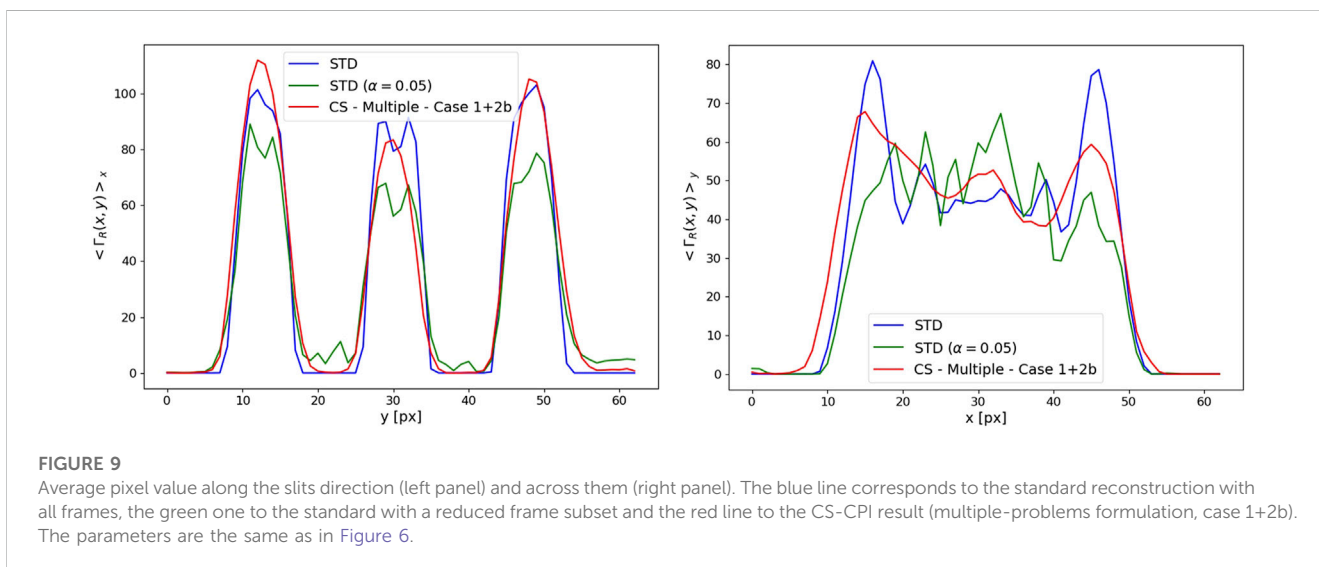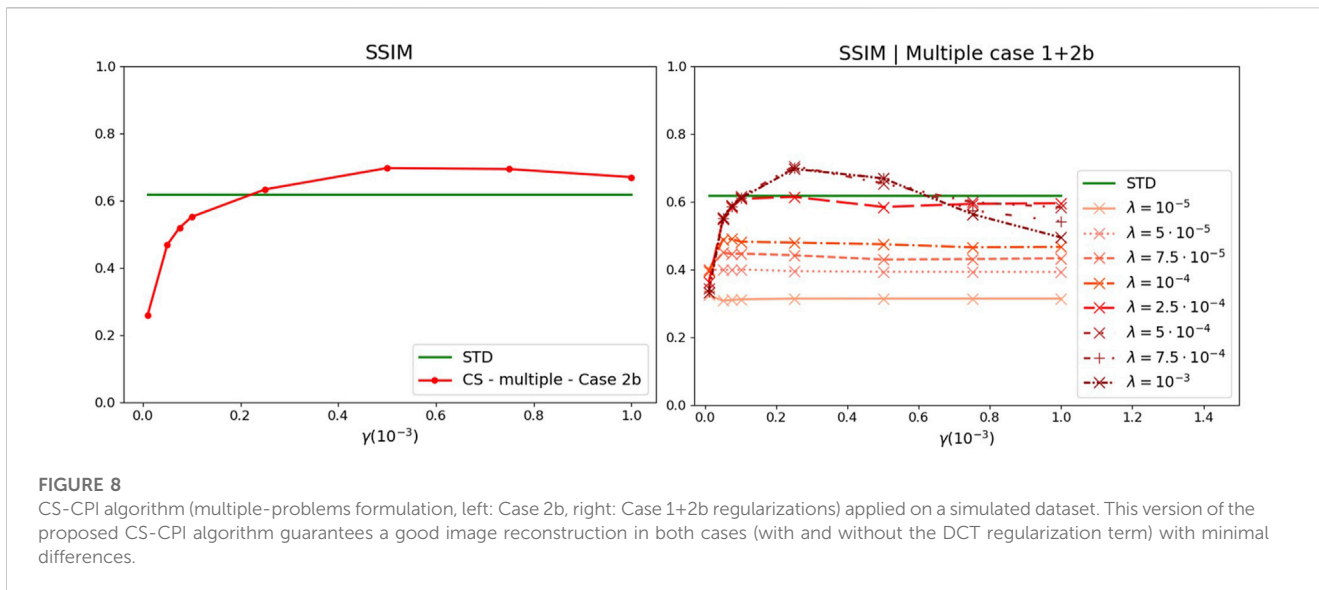

FIGURE 7
CS-CPI algorithm (single-problem formulation, left: Case 2b, right: Case 1+2b regularizations) applied on a simulated dataset. This version of the proposed CS-CPI algorithm succeeds in the reconstruction if both regularization terms are included in a certain range of the regularization parameters λ and γ.

by at least 3 times. Thereby, in the rest of this paragraph we will concentrate on case 2b. The best image reconstructions in the four cases described above are reported in Figure 6, see the caption for details on the parameters values.

As evident from Figures 7, 8, all the versions of the CS-CPI algorithm with single-problem and multiple-problems approaches improve image quality (except for Case 2b in the single-problem formulation whose results are comparable with the standard correlation case) with the Case 1+2b (single-problem

formulation) giving the best results in terms of reconstruction quality.

Comparing the results reported in Figure 4 with Figure 7, as well as the results from Figure 5 with Figure 8, it emerges that the introduction of a regularization term requiring gradient sparsity enhances reconstruction quality, since it tends to penalize fast noise fluctuations in the background, limiting at the same time the introduction of artifacts. Reconstruction capability is further enhanced when the requests of sparsity in the gradient and the

FIGURE 8
CS-CPI algorithm (multiple-problems formulation, left: Case 2b, right: Case 1+2b regularizations) applied on a simulated dataset. This version of the proposed CS-CPI algorithm guarantees a good image reconstruction in both cases (with and without the DCT regularization term) with minimal differences.

FIGURE 9
Average pixel value along the slits direction (left panel) and across them (right panel). The blue line corresponds to the standard reconstruction with all frames, the green one to the standard with a reduced frame subset and the red line to the CS-CPI result (multiple-problems formulation, case 1+2b). The parameters are the same as in Figure 6.

transform domains are combined. In particular, the most promising results are observed in Case 1+2b (single-problem formulation). However, it is worth noticing that the single-problem formulation of the CS-CPI algorithms provides satisfactory results also in its simpler formulation (Case 1). Instead, when analyzing the results of the multiple-problems strategy, the presence of a term penalizing the image gradients seems crucial. Actually, while the multiple-problems approach to CS-CPI is not able to provide a satisfactory reconstruction, as shown in Figure 5, introducing a TV-related term (the image Laplacian) reverses the situation. From an overall comparison involving single- or multiple-problems strategies, as well as all the considered regularization term, it emerges that the best results are obtained when both the DCT and the Laplacian of the target image are regularized.

We conclude by showing in Figure 9 the average pixel value along the slit direction and across them. The contrast obtained in the CS-TV case, corresponding to the multiple-problems formulation with the DCT and the Laplacian regularization terms, is always higher than in the correlation-based reconstruction obtained with the same frame subset, while it is comparable with the correlation-based ground truth, obtained with all the available frames.

4 Conclusion

CPI is a novel technique capable of acquiring the light field, the combined information of intensity and propagation direction of light. The standard image retrieval is performed by evaluating correlations between the intensities measured by two detectors with spatial resolution. In this work, we have discussed a first demonstration of the applicability of CS-based approaches to CPI. We have explored several possibilities for building the objective function. Specifically, we have tested two approaches: one envisaging a single-problem formulation, in which the whole information on the object coming from all light propagation directions is exploited at once, and the other a multi-problem approach, in which reconstruction is separately

performed for the object illuminated by different source points. Besides, we have considered regularization terms promoting both the sparsity of the image DCT and the sparsity of the image gradient, showing that, at a fixed frame number, CS-based approaches can boost the CPI image quality with respect to the deterministic correlation measurement, thus allowing for shorter acquisition times. Nevertheless, the high computational costs usually associated with common CS implementations still represent a bottleneck towards the extensive application of the selected solution into the operational CPI framework.

Data availability statement

The raw data supporting the conclusion of this article will be made available by the authors, without undue reservation.

Author contributions

IP: Conceptualization, Formal Analysis, Methodology, Software, Writing–original draft, Writing–review and editing. FSa: Conceptualization, Software, Writing–review and editing. GM: Data curation, Software, Writing–review and editing. FSc: Writing–original draft, Writing–review and editing. FP: Conceptualization, Writing–original draft, Writing–review and editing. FM: Conceptualization, Methodology, Writing–review and editing. MI: Funding acquisition, Writing–review and editing. GF: Validation, Writing–review and editing. DM: Validation, Writing–review and editing. NP: Validation, Writing–review and editing. CA: Supervision, Writing–review and editing. MD'A: Funding acquisition, Project administration, Supervision, Writing–review and editing.

Funding

Conflict of interest

Authors IP, FSa and CA were employed by the company Planetek Italia s.r.l. Authors MI, GF, DM, NP were employed by the company Planetek Hellas E.P.E.

The remaining authors declare that the research was conducted in the absence of any commercial or financial relationships that could be construed as a potential conflict of interest.

Publisher's note

All claims expressed in this article are solely those of the authors and do not necessarily represent those of their affiliated organizations, or those of the publisher, the editors and the reviewers. Any product that may be evaluated in this article, or claim that may be made by its manufacturer, is not guaranteed or endorsed by the publisher.

References

1. D'Angelo M, Pepe FV, Garuccio A, Scarcelli G. Correlation plenoptic imaging. *Phys Rev Lett* (2016) 116:223602. doi:10.1103/physrevlett.116.223602

2. Pepe FV, Di Lena F, Garuccio A, Scarcelli G, D'Angelo M. Correlation plenoptic imaging with entangled photons. *Technologies* (2016) 4:17. doi:10.3390/technologies4020017

3. Pepe FV, Di Lena F, Mazzilli A, Edrei E, Garuccio A, Scarcelli G, et al. Diffraction-limited plenoptic imaging with correlated light. *Phys Rev Lett* (2017) 119:243602. doi:10.1103/physrevlett.119.243602

4. Di Lena F, Pepe FV, Garuccio A, D'Angelo M. Correlation plenoptic imaging: an overview. *Appl Sci* (2018) 8:1958. doi:10.3390/app8101958

5. Di Lena F, Massaro G, Lupo A, Garuccio A, Pepe FV, D'Angelo M. Correlation plenoptic imaging between arbitrary planes. *Opt Express* (2020) 28:35857–68. doi:10.1364/oe.404464

6. Scagliola A, Di Lena F, Garuccio A, D'Angelo M, Pepe FV. Correlation plenoptic imaging for microscopy applications. *Phys Lett A* (2020) 384:126472. doi:10.1016/j.physleta.2020.126472

7. Massaro G, Giannella D, Scagliola A, Di Lena F, Scarcelli G, Garuccio A, et al. Light-field microscopy with correlated beams for high-resolution volumetric imaging. *Scientific Rep* (2022) 12:16823. doi:10.1038/s41598-022-21240-1

8. Massaro G, Di Lena F, D'Angelo M, Pepe FV. Effect of finite-sized optical components and pixels on light-field imaging through correlated light. *Sensors* (2022) 22:2778. doi:10.3390/s22072778

9. Massaro G, Mos P, Vasiukov S, Di Lena F, Scattarella F, Pepe FV, et al. Correlated-photon imaging at 10 volumetric images per second. *Scientific Rep* (2023) 13:12813. doi:10.1038/s41598-023-39416-8

10. Adelson EH, Wang JY. Single lens stereo with a plenoptic camera. *IEEE Trans pattern Anal machine intelligence* (1992) 14:99–106. doi:10.1109/34.121783

11. Ng R, Levoy M, Brédif M, Duval G, Horowitz M, Hanrahan P. Light field photography with a hand-held plenoptic camera. *Computer Sci Tech Rep CSTR* (2005) 2:1–11.

12. Ng R. Fourier slice photography. *ACM Trans Graphics* (2005) 24:735–44. doi:10.1145/1073204.1073256

13. Ng R. *Digital light field photography*. California: Stanford University (2006).

14. Georgiev T, Intwala C. *Light field camera design for integral view photography*. San Jose, California: Adobe System, Inc. (2006). *Technical Report*.

15. Georgeiv T, Zheng KC, Curless B, Salesin D, Nayar S, Intwala C (2006). Spatio-angular resolution tradeoffs in integral photography. In Proceedings of the 17th

Eurographics Conference on Rendering Techniques (Goslar, DEU: Eurographics Association), EGSR '06, 263–72. Goslar, Germany, June 2006.

16. Georgiev TG, Lumsdaine A. Focused plenoptic camera and rendering. *J Electron Imaging* (2010) 19:021106. doi:10.1117/1.3442712

17. Dansereau DG, Pizarro O, Williams SB (2013). Decoding, calibration and rectification for lenselet-based plenoptic cameras. In Proceedings of the IEEE conference on computer vision and pattern recognition. 1027–34. Portland, OR, USA, June 2013.

18. Broxton M, Grosenick L, Yang S, Cohen N, Andalman A, Deisseroth K, et al. Wave optics theory and 3-D deconvolution for the light field microscope. *Opt Express* (2013) 21:25418–39. doi:10.1364/oe.21.025418

19. Pittman TB, Shih Y-H, Strekalov DV, Sergienko AV. Optical imaging by means of two-photon quantum entanglement. *Phys Rev A* (1995) 52:R3429–32. doi:10.1103/physreva.52.r3429

20. Pittman T, Strekalov D, Klyshko D, Rubin M, Sergienko A, Shih Y. Two-photon geometric optics. *Phys Rev A* (1996) 53:2804–15. doi:10.1103/physreva.53.2804

21. Bennink RS, Bentley SJ, Boyd RW, Howell JC. Quantum and classical coincidence imaging. *Phys Rev Lett* (2004) 92:033601. doi:10.1103/physrevlett.92.033601

22. Bennink RS, Bentley SJ, Boyd RW. "Two-photon" coincidence imaging with a classical source. *Phys Rev Lett* (2002) 89:113601. doi:10.1103/physrevlett.89.113601

23. Valencia A, Scarcelli G, D'Angelo M, Shih Y. Two-photon imaging with thermal light. *Phys Rev Lett* (2005) 94:063601. doi:10.1103/physrevlett.94.063601

24. Scarcelli G, Berardi V, Shih Y. Can two-photon correlation of chaotic light be considered as correlation of intensity fluctuations? *Phys Rev Lett* (2006) 96:063602. doi:10.1103/physrevlett.96.063602

25. Gatti A, Brambilla E, Bache M, Lugiato LA. Ghost imaging with thermal light: comparing entanglement and classical correlation. *Phys Rev Lett* (2004) 93:093602. doi:10.1103/physrevlett.93.093602

26. Ferri F, Magatti D, Gatti A, Bache M, Brambilla E, Lugiato LA. High-resolution ghost image and ghost diffraction experiments with thermal light. *Phys Rev Lett* (2005) 94:183602. doi:10.1103/physrevlett.94.183602

27. O'Sullivan MN, Chan KWC, Boyd RW. Comparison of the signal-to-noise characteristics of quantum versus thermal ghost imaging. *Phys Rev A* (2010) 82:053803. doi:10.1103/physreva.82.053803

28. Scala G, D'Angelo M, Garuccio A, Pascazio S, Pepe FV. Signal-to-noise properties of correlation plenoptic imaging with chaotic light. *Phys Rev A* (2019) 99:053808. doi:10.1103/physreva.99.053808

29. Massaro G, Scala G, D'Angelo M, Pepe FV. Comparative analysis of signal-to-noise ratio in correlation plenoptic imaging architectures. *The Eur Phys J Plus* (2022) 137:1123. doi:10.1140/epjp/s13360-022-03295-1

30. Katz O, Bromberg Y, Silberberg Y. Compressive ghost imaging. *Appl Phys Lett* (2009) 95:131110. doi:10.1063/1.3238296

31. Jiying L, Jubo Z, Chuan L, Shisheng H. High-quality quantum-imaging algorithm and experiment based on compressive sensing. *Opt Lett* (2010) 35:1206–8. doi:10.1364/ol.35.001206

32. Candes E, Romberg J, Tao T. Robust uncertainty principles: exact signal reconstruction from highly incomplete frequency information. *IEEE Trans Inf Theor* (2006) 52:489–509. doi:10.1109/tit.2005.862083

33. Candès EJ, Romberg JK, Tao T. Stable signal recovery from incomplete and inaccurate measurements. *Commun Pure Appl Math* (2006) 59:1207–23. doi:10.1002/cpa.20124

34. Candes EJ, Wakin MB. An introduction to compressive sampling. *IEEE Signal Process. Mag* (2008) 25:21–30. doi:10.1109/msp.2007.914731

35. Donoho DL. Compressed sensing. *IEEE Trans Inf Theor* (2006) 52:1289–306. doi:10.1109/tit.2006.871582

36. Massaro G, Pepe FV, D'Angelo M. Refocusing algorithm for correlation plenoptic imaging. *Sensors* (2022) 22:6665. doi:10.3390/s22176665

37. Ferri F, Magatti D, Lugiato L, Gatti A. Differential ghost imaging. *Phys Rev Lett* (2010) 104:253603. doi:10.1103/physrevlett.104.253603

38. Olshausen BA, Field DJ. Natural image statistics and efficient coding. *Netw Comput Neural Syst* (1996) 7:333–9. doi:10.1088/0954-898x_7_2_014

39. Zhu R, Li G, Guo Y. Compressed-sensing-based gradient reconstruction for ghost imaging. *Int J Theor Phys* (2019) 58:1215–26. doi:10.1007/s10773-019-04013-x

40. Liang Z, Yu D, Cheng Z, Zhai X, Hu Y. Compressed sensing fourier single pixel imaging algorithm based on joint discrete gradient and non-local self-similarity priors. *Opt Quan Electro* (2020) 52:376. doi:10.1007/s11082-020-02501-7

41. Yi C, Zhengdong C, Xiang F, Yubao C, Zhenyu L. Compressive sensing ghost imaging based on image gradient. *Optik* (2019) 182:1021–9. doi:10.1016/j.ijleo.2019.01.067

42. Rudin LI, Osher S, Fatemi E. Nonlinear total variation based noise removal algorithms. *Physica D: Nonlinear Phenomena* (1992) 60:259–68. doi:10.1016/0167-2789(92)90242-F

43. Lou Y, Zeng T, Osher S, Xin J. A weighted difference of anisotropic and isotropic total variation model for image processing. *SIAM J Imaging Sci* (2015) 8:1798–823. doi:10.1137/14098435X

44. Kim Y, Kudo H. Nonlocal total variation using the first and second order derivatives and its application to ct image reconstruction. *Sensors* (2020) 20:3494. doi:10.3390/s20123494

45. Friedman J, Hastie T, Tibshirani R. Regularization paths for generalized linear models via coordinate descent. *J Stat Softw* (2010) 33:1–22. doi:10.18637/jss.v033.i01

46. Wang Z, Bovik A, Sheikh H, Simoncelli E. Image quality assessment: from error visibility to structural similarity. *IEEE Trans Image Process* (2004) 13:600–12. doi:10.1109/TIP.2003.819861

47. Yang D, Chang C, Wu G, Luo B, Yin L. Compressive ghost imaging of the moving object using the low-order moments. *Appl Sci* (2020) 10:7941. doi:10.3390/app10217941